

# Oxygen Nonstoichiometry, Mixed Conductivity, and Mössbauer Spectra of $\text{Ln}_{0.5}\text{A}_{0.5}\text{FeO}_{3-\delta}$ ( $\text{Ln} = \text{La}–\text{Sm}$ , $\text{A} = \text{Sr}$ , $\text{Ba}$ ): Effects of Cation Size

Vladislav V. Kharton,<sup>\*,†</sup> Andrei V. Kovalevsky,<sup>†,‡</sup> Mikhail V. Patrakeev,<sup>§</sup>  
Ekaterina V. Tsipis,<sup>†,||</sup> Alexandre P. Viskup,<sup>⊥</sup> Vladislav A. Kolotygin,<sup>†</sup>  
Aleksy A. Yaremchenko,<sup>†</sup> Aliaksandr L. Shaula,<sup>†,#</sup> Evgeny A. Kiselev,<sup>†</sup> and  
João C. Waerenborgh<sup>||</sup>

Department of Ceramics and Glass Engineering, CICECO, University of Aveiro,  
3810-193 Aveiro, Portugal, Materials Department, Flemish Institute for Technological Research (VITO),  
2400 Mol, Belgium, Institute of Solid State Chemistry, Ural Division of RAS, 91 Pervomayskaya Str.,  
Ekaterinburg 620219, Russia, Chemistry Department, Instituto Tecnológico e Nuclear, CFMC-UL, EN 10,  
2686-953 Sacavém, Portugal, Institute of Physicochemical Problems, Belarus State University,  
14 Leningradskaya Str., 220050 Minsk, Belarus, and Department of Mechanical Engineering,  
SEG-CEMUC, University of Coimbra, P-3030-788 Coimbra, Portugal

Received June 10, 2008. Revised Manuscript Received September 3, 2008

Increasing the difference of the  $\text{Ln}^{3+}$  and  $\text{A}^{2+}$  cation radii in perovskite-type  $\text{Ln}_{0.5}\text{A}_{0.5}\text{FeO}_{3-\delta}$  ( $\text{Ln} = \text{La}$ ,  $\text{Pr}$ ,  $\text{Nd}$ ,  $\text{Sm}$ ;  $\text{A} = \text{Sr}$ ,  $\text{Ba}$ ) results in higher oxygen deficiency and lower oxygen-ionic and p-type electronic conductivities, determined using the oxygen permeation and total conductivity measurements at 973–1223 K. The relationships between the anion transport and A-site cation size mismatch remain essentially similar in air and under reducing conditions when most iron cations become trivalent, thus confirming critical influence of oxygen-vacancy trapping processes induced by the lattice strain. At low temperatures, analogous correlation is also observed for quadrupole splittings derived from the Mössbauer spectra of oxygen-stoichiometric  $\text{Ln}_{0.5}\text{A}_{0.5}\text{FeO}_3$ . Contrary to the ionic conductivity variations, the role of surface exchange kinetics as a permeation-limiting factor, evaluated from the membrane thickness dependence of oxygen fluxes, tends to decrease on  $\text{Ba}^{2+}$  doping and on decreasing  $\text{Ln}^{3+}$  size in  $\text{Ln}_{0.5}\text{Sr}_{0.5}\text{FeO}_{3-\delta}$  series. The n-type electronic conduction and low- $p(\text{O}_2)$  stability at 1223 K are substantially unaffected by the cation radius mismatch.

## 1. Introduction

As a result of substantially high mixed conductivity and stability, iron-containing oxide phases with  $\text{ABO}_3$  perovskite structure are of great interest for the applications in solid oxide fuel cell (SOFC) cathodes, dense ceramic membranes

for oxygen separation and partial oxidation of natural gas, and catalyst supports.<sup>1–8</sup> One promising group of the ferrite materials is based on perovskite-type  $\text{La}_{1-x}\text{Sr}_x\text{FeO}_{3-\delta}$  where the highest level of electronic and oxygen-ionic transport is observed at  $x \approx 0.5$ .<sup>6–8</sup> While moderate acceptor-type doping enhances the concentrations of mobile oxygen vacancies and p-type electronic charge carriers in  $(\text{La},\text{Sr})\text{FeO}_{3-\delta}$ , increasing  $\text{Sr}^{2+}$  content above 50% promotes vacancy-ordering and hole localization processes, with a negative impact on the transport properties. Taking into account the relatively low costs of mixed rare-earth precursors, significant economical benefits are expected when replacing  $\text{La}^{3+}$  with mixtures of lanthanide ( $\text{Ln}^{3+}$ ) cations.<sup>1,9</sup> However, information on the relationships between A-site cation radius, oxygen anion conduction, and surface exchange-related processes in the perovskite-like ferrites is very scarce.

In the case of perovskite cobaltites, gallates, and aluminates, the oxygen-ionic conductivity tends to decrease with decreasing  $\text{Ln}^{3+}$  size; similar trends are also observed for nickelates and cuprates with  $\text{K}_2\text{NiF}_4$ -type structure (e.g., refs 10–15 and references cited therein). This behavior was

\* Corresponding author. Tel: +351-234-370263. Fax: +351-234-425300. E-mail: kharton@ua.pt.

† University of Aveiro.

‡ Flemish Institute for Technological Research (VITO).

§ Ural Division of RAS.

|| Instituto Tecnológico e Nuclear.

⊥ Belarus State University.

# University of Coimbra.

- (1) Simner, S. P.; Bonnett, J. F.; Canfield, N. L.; Meinhardt, K. D.; Shelton, J. P.; Sprenkle, V. L.; Stevenson, J. W. *J. Power Sources* **2003**, *113*, 1.
- (2) Lu, X.; Liu, M. In *Solid State Ionic Devices*; Wachsmann, E., Akridge, J. R., Liu, M., Yamazoe, N., Eds.; The Electrochemical Society: Pennington, NJ, 1999; PV99-13, p 139.
- (3) Yoo, J.; Verma, A.; Wang, S.; Jacobson, A. J. *J. Electrochem. Soc.* **2005**, *152*, A497.
- (4) Mai, A.; Haanappel, V. A. C.; Uhlenbruck, S.; Tietz, F.; Stöver, D. *Solid State Ionics* **2005**, *176*, 1341.
- (5) Ralph, J. M.; Rossignol, C.; Kumar, R. *J. Electrochem. Soc.* **2003**, *150*, A1518.
- (6) Bahteeva, J. A.; Leonidov, I. A.; Patrakeev, M. V.; Mitberg, E. B.; Kozhevnikov, V. L.; Poeppelmeier, K. R. *J. Solid State Electrochem.* **2004**, *8*, 578.
- (7) Diethelm, S.; Van herle, J.; Sfeir, J.; Buffat, P. *J. Eur. Ceram. Soc.* **2005**, *25*, 2191.
- (8) Tsipis, E. V.; Patrakeev, M. V.; Kharton, V. V.; Yaremchenko, A. A.; Mather, G. C.; Shaula, A. L.; Leonidov, I. A.; Kozhevnikov, V. L.; Frade, J. R. *Solid State Sci.* **2005**, *7*, 355.

(9) Carolan, M. F.; Dyer, P. N.; Motika, S. A.; Alba, P. B. Fluid separation devices capable of operating under high carbon dioxide partial pressures. U.S. Patent 6056807, 2000.

(10) Kilner, J. A. *Solid State Ionics* **2000**, *129*, 13.

ascribed to various factors, in particular, the lattice strains caused by the  $\text{Ln}^{3+}$  and  $\text{A}^{2+}$  radius mismatch,<sup>10,12</sup> deviations of the perovskite structure tolerance factor from an optimum value,<sup>11</sup> effects of the cation polarizability on the oxygen–metal binding energy,<sup>13–15</sup> and variations in the lattice free volume and in the diameter of ion migration channels (so-called “bottlenecks”).<sup>10–13</sup> One hypothesis explaining the influence of local strains, which originate from differences in  $\text{Ln}^{3+}$  and  $\text{A}^{2+}$  radii, refers to the formation of point-defect clusters involving the oxygen vacancies.<sup>10</sup> Irrespective of the defect association mechanisms, the highest ionic conductivity is often observed when the values of the perovskite tolerance factor are approximately 0.96–0.97, in correlation with the orthorhombic to rhombohedral phase transition and resultant lattice instability.<sup>11,16</sup> On the contrary, an enhanced oxygen-exchange kinetics and lowest polarization resistance of the porous SOFC electrodes are characteristic of perovskite-related materials containing either  $\text{Ba}^{2+}$  or lanthanide cations with moderate radius ( $\text{Ln} = \text{Pr}–\text{Sm}$ ).<sup>17–21</sup> The latter tendency known for manganite-, ferrite-, cobaltite-, and nickelate-based systems<sup>17–21</sup> may indicate a significant role of specific catalytic properties of the lanthanide cations or small surface clusters and secondary phases comprising  $\text{Ln}^{3+}$ .<sup>18,19</sup> At the same time, the electrochemical behavior of porous electrodes is strongly dependent on their interaction with solid oxide electrolyte, affected by the A-site cation radius and perovskite phase stability;<sup>17</sup> this factor may hamper any precise extraction of the electrode surface-related contributions from total polarization resistance.

The present work is focused on the analysis of oxygen nonstoichiometry, ionic transport, and electronic conductivity in  $\text{Ln}_{0.5}\text{A}_{0.5}\text{FeO}_{3-\delta}$  ( $\text{Ln} = \text{La}–\text{Sm}$ ;  $\text{A} = \text{Sr}, \text{Ba}$ ) as a function of the cation size. To assess the iron oxidation states and structural strains at low temperatures, Mössbauer spectroscopy was employed. Most data on  $\text{La}_{0.5}\text{Sr}_{0.5}\text{FeO}_{3-\delta}$  and  $\text{Pr}_{0.5}\text{Sr}_{0.5}\text{FeO}_{3-\delta}$ , reported elsewhere,<sup>6,22,23</sup> were recollected and reanalyzed; these data are used in the present work for the sake of comparative analysis.

**Table 1. Properties<sup>a</sup> of As-Prepared  $\text{Ln}_{0.5}\text{A}_{0.5}\text{FeO}_3$  Equilibrated with Atmospheric Oxygen**

composition	space group	tolerance factor <sup>b</sup>	unit cell parameter			$(3 - \delta)^c$
			<i>a</i> , nm	<i>b</i> , nm	<i>c</i> , nm	
$\text{La}_{0.5}\text{Sr}_{0.5}\text{FeO}_{3-\delta}$	<i>R</i> 3 <i>c</i>	0.983	0.55150(4)		1.34287(9)	$3.00 \pm 0.01$
$\text{Pr}_{0.5}\text{Sr}_{0.5}\text{FeO}_{3-\delta}$	<i>Imma</i>	<sup>d</sup>	0.54681(1)	0.77321(1)	0.55049(1)	$3.02 \pm 0.02$
$\text{Nd}_{0.5}\text{Sr}_{0.5}\text{FeO}_{3-\delta}$	<i>Pbnm</i>	0.967	0.54978(4)	0.54737(4)	0.77447(6)	$3.00 \pm 0.01$
$\text{Sm}_{0.5}\text{Sr}_{0.5}\text{FeO}_{3-\delta}$	<i>Pbnm</i>	0.962	0.54622(1)	0.54627(4)	0.77249(1)	$2.99 \pm 0.01$
$\text{La}_{0.5}\text{Ba}_{0.5}\text{FeO}_{3-\delta}$	<i>Pm</i> 3 <i>m</i>	1.012	0.39413(4)			$3.01 \pm 0.01$

<sup>a</sup> All data correspond to room temperature. <sup>b</sup> The A-site cation radius values<sup>24</sup> correspond to 12-fold coordination. <sup>c</sup> The oxygen content at room temperature and the corresponding statistical error were calculated from TGA and iodometric titration results. <sup>d</sup> The A-site cation radius for 12-fold coordination is not available.

## 2. Experimental Section

Single-phase ceramic samples of perovskite-type  $\text{La}_{0.5}\text{Ba}_{0.5}\text{FeO}_{3-\delta}$  and  $\text{Ln}_{0.5}\text{Sr}_{0.5}\text{FeO}_{3-\delta}$  ( $\text{Ln} = \text{La}, \text{Pr}, \text{Nd}, \text{and Sm}$ ) with 93–97% density were prepared via glycine-nitrate synthesis route with sintering at 1530–1790 K in air. The glycine-nitrate synthesis procedure was similar to that described elsewhere.<sup>22,23</sup> After sintering, all materials were annealed at 1250–1300 K in air and slowly cooled to achieve equilibrium oxygen content at low temperatures. The powdered samples used for X-ray diffraction (XRD) analysis, iodometric titration, Mössbauer spectroscopy, coulometric titration, and thermogravimetric analysis (TGA) were prepared by grinding of dense ceramics. XRD analysis confirmed the formation of single perovskite phases. The room-temperature structural data on  $\text{Ln}_{0.5}\text{A}_{0.5}\text{FeO}_3$  equilibrated with atmospheric oxygen are summarized in Table 1; Figure 1A presents one example of the observed, calculated, and difference XRD patterns. The overall cation composition of selected ceramic samples was verified by ion-coupled plasma (ICP) spectroscopic analysis using a Jobin Yvon instrument, model JY 70 plus. In all cases, the deviations from nominal cation composition were lower than 0.1 atom %, comparable to the experimental error; the total amount of impurity cations did not exceed 0.02 atom %. Energy-dispersive spectroscopy (EDS) showed an absence of compositional inhomogeneities in the ceramic materials within the limits of experimental uncertainty. Additional series of ceramic samples used for the analysis of phase composition at elevated temperatures were annealed in various atmospheres and then quenched in liquid nitrogen. This method was used, in particular, to confirm the perovskite phase stability limits discussed below; as an example, Figure 1B displays the XRD pattern of  $\text{La}_{0.5}\text{Ba}_{0.5}\text{FeO}_{3-\delta}$ , reduced at 1023 K and  $p(\text{O}_2) = 2 \times 10^{-19}$  atm. The experimental procedures and equipment used for materials characterization were described elsewhere.<sup>6,8,14–16,18,22,23,25,26</sup>

The Mössbauer spectra were collected at 4.1 K (with samples immersed in liquid He) and 297 K on a conventional transmission constant-acceleration spectrometer with a 25 mCi <sup>57</sup>Co (Rh) source.<sup>23</sup> The room-temperature spectra were fitted to Lorentzian lines using a nonlinear least-squares method; the relative areas and widths of both peaks in a quadrupole doublet were kept equal during refinement. The magnetically split spectra collected at 4.1 K were fitted with a distributions of magnetic sextets according to the histogram method.<sup>27</sup>

- (11) Hayashi, H.; Inaba, H.; Matsuyama, M.; Lan, N. G.; Dokiya, M.; Tagawa, H. *Solid State Ionics* **1999**, *122*, 1.
- (12) Mogensen, M.; Luby, D.; Bonanos, N.; Hendriksen, P. V.; Poulsen, F. W. *Solid State Ionics* **2004**, *174*, 279.
- (13) Sammells, A. F.; Cook, R. L.; White, J. H.; Osborne, J. J.; MacDuff, R. C. *Solid State Ionics* **1992**, *52*, 111.
- (14) Kharton, V. V.; Naumovich, E. N.; Vechev, A. A.; Nikolaev, A. V. *J. Solid State Chem.* **1995**, *120*, 128.
- (15) Kharton, V. V.; Viskup, A. V.; Kovalevsky, A. P.; Naumovich, E. N.; Marques, F. M. B. *Solid State Ionics* **2001**, *143*, 337.
- (16) Vyshatko, N. P.; Kharton, V.; Shaulo, A. L.; Naumovich, E. N.; Marques, F. *Mater. Res. Bull.* **2003**, *38*, 185.
- (17) Sakaki, Y.; Takeda, Y.; Kato, A.; Imanishi, N.; Yamamoto, O.; Hattori, M.; Iio, M.; Esaki, Y. *Solid State Ionics* **1999**, *118*, 187.
- (18) Kovalevsky, A. V.; Kharton, V. V.; Yaremchenko, A. A.; Pivak, Y. V.; Tsipis, E. V.; Yakovlev, S. O.; Markov, A. A.; Naumovich, E. N.; Frade, J. R. *J. Electroceram.* **2007**, *18*, 205.
- (19) Serra, J. M.; Vert, V. B.; Betz, M.; Haanappel, V. A. C.; Meulenberg, W. A.; Tietz, F. *J. Electrochem. Soc.* **2008**, *155*, B207.
- (20) Baumann, F. S.; Fleig, J.; Cristiani, G.; Stuhlhofer, B.; Habermeier, H.-U.; Maier, J. *J. Electrochem. Soc.* **2007**, *154*, B931.
- (21) Ishihara, T.; Fukui, S.; Nishiguchi, H.; Takita, Y. *Solid State Ionics* **2002**, *152–153*, 609.
- (22) Kharton, V. V.; Patrakee, M. V.; Waerenborgh, J. C.; Kovalevsky, A. V.; Pivak, Y. V.; Gaczyński, P.; Markov, A. A.; Yaremchenko, A. A. *J. Phys. Chem. Solids* **2007**, *68*, 355.
- (23) Kharton, V. V.; Waerenborgh, J. C.; Viskup, A. P.; Yakovlev, S.; Patrakee, M. V.; Gaczyński, P.; Marozau, I. P.; Yaremchenko, A. A.; Shaulo, A. L.; Samakhval, V. V. *J. Solid State Chem.* **2006**, *179*, 1273.

- (24) Shannon, R. D. *Acta Crystallogr., Sect. A* **1976**, *32*, 751.
- (25) Patrakee, M. V.; Mitberg, E. B.; Lakhtin, A. A.; Leonidov, I. A.; Kozhevnikov, V. L.; Kharton, V. V.; Avdeev, M.; Marques, F. M. B. *J. Solid State Chem.* **2002**, *167*, 203.
- (26) Kharton, V. V.; Tikhonovich, V. N.; Shuangbao, L.; Naumovich, E. N.; Kovalevsky, A. V.; Viskup, A. P.; Bashmakov, I. A.; Yaremchenko, A. A. *J. Electrochem. Soc.* **1998**, *145*, 1363.
- (27) Hesse, J.; Rübartsch, A. *J. Phys. E* **1974**, *7*, 526.

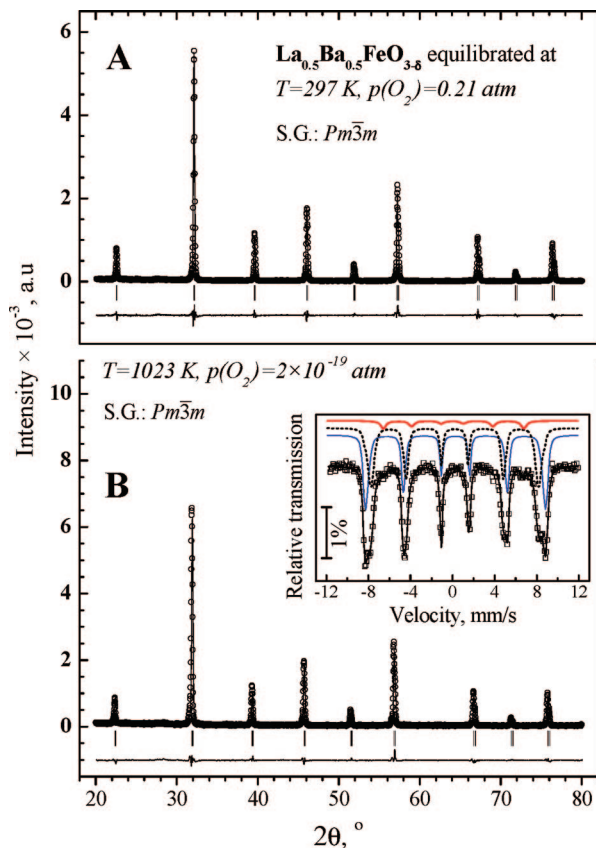


**Figure 1.** Observed, calculated and difference room-temperature XRD patterns of La<sub>0.5</sub>Ba<sub>0.5</sub>FeO<sub>3-δ</sub>, equilibrated with atmospheric oxygen at low temperatures (A) and reduced at  $p(\text{O}_2) = 2 \times 10^{-19}$  atm and 1023 K (B). Inset shows the room-temperature Mössbauer spectrum of reduced La<sub>0.5</sub>Ba<sub>0.5</sub>FeO<sub>3-δ</sub>; the curves plotted on the experimental points are the sum of three distributions of magnetic sextets attributed to hexa-, penta-, and tetra-coordinated Fe<sup>3+</sup>, all shown slightly shifted for clarity.

Detailed description of the experimental techniques employed to measure total conductivity ( $\sigma$ , 4-probe DC) and equilibrium oxygen nonstoichiometry ( $\delta$ ) as a function of the oxygen partial pressure and temperature and to determine oxygen permeation fluxes ( $j$ ) through dense ferrite membranes placed under an oxygen chemical potential gradient can be found in previous publications.<sup>6,23,25,26</sup> For all permeation data presented in this work, the oxygen partial pressure at the membrane feed side ( $p_2$ ) was equal to 0.21 atm; the permeate-side oxygen pressure ( $p_1$ ) and membrane thickness ( $d$ ) varied in the ranges  $1.5 \times 10^{-2}$  to 0.20 atm and 0.60–1.60 mm, respectively. Prior to the permeation tests, all membranes were polished with diamond pastes down to a particle size of 1  $\mu\text{m}$  and then annealed at 1320–1340 K for 15–20 min to provide similar roughness of the membrane surfaces. For each composition, no less than 3–4 membranes were studied. The reproducibility error of the oxygen permeation fluxes at 1123–1223 K was less than 5%; at lower temperatures when vacancy-ordering processes in the ferrite lattices become significant, this error achieved 15%. The reproducibility error of the partial ionic conductivity ( $\sigma_0$ ) values in reducing atmospheres, calculated from  $p(\text{O}_2)$ -dependencies of the total conductivity as explained below, was lower than 12%. The relative error of the total conductivity measurements was approximately 2%. For the room-temperature oxygen content measured by TGA and iodometric titration, the absolute error was relatively high, 0.01–0.02 atoms per formula unit (Table 1); these uncertainties are primarily associated with hydration and adsorption of other species from the gaseous phase at low temperatures. At high temperatures, the reproducibility error

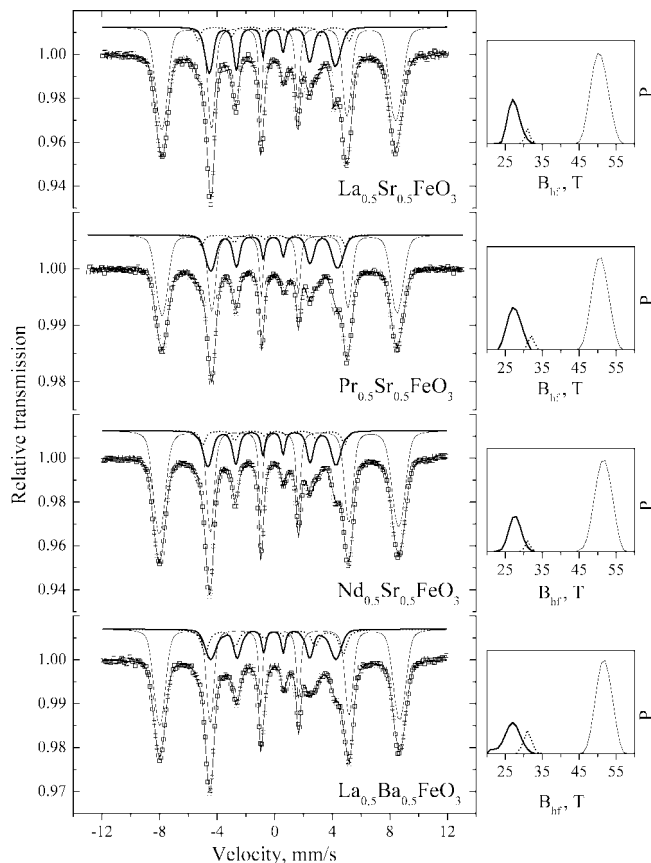


**Figure 2.** Mössbauer spectra of Ln<sub>0.5</sub>A<sub>0.5</sub>FeO<sub>3</sub> equilibrated with atmospheric oxygen at low temperatures, taken at 4.1 K. The line on the experimental points is the sum of three distributions of magnetic sextets corresponding to octahedrally coordinated Fe<sup>3+</sup>, Fe<sup>5+</sup>, and localized Fe<sup>4+</sup>, shown slightly shifted for clarity. The probability distributions ( $P$ ) of the magnetic hyperfine fields are shown on the right-hand side of the corresponding spectra.

of  $\delta$  values determined by the coulometric titration in combination with TGA was lower than  $\pm 0.003$ .

### 3. Results and Discussion

**3.1. Mössbauer Spectroscopy.** The 4.1 K Mössbauer spectra of Ln<sub>0.5</sub>A<sub>0.5</sub>FeO<sub>3</sub> equilibrated with atmospheric oxygen under ambient conditions are presented in Figure 2. These spectra collected far below the Néel temperature ( $T_N$ ) are all similar to one another and to those reported for La<sub>0.5</sub>A<sub>0.5</sub>FeO<sub>3</sub>.<sup>28,29</sup> For most (Ln,A)FeO<sub>3</sub> systems, a complete nominal disproportionation of Fe<sup>4+</sup> into Fe<sup>3+</sup> and Fe<sup>5+</sup> is usually suggested in this temperature range.<sup>28–32</sup> The spectra of La<sub>0.5</sub>Sr<sub>0.5</sub>FeO<sub>3</sub> might also be fitted to two contributions with the parameters characteristic of Fe<sup>3+</sup> and Fe<sup>5+</sup>.<sup>22,28</sup> However, this model ignores one shoulder at a Doppler velocity of approximately +3 mm/s and poorly describes another peak at –3 mm/s, marked by the arrows in Figure

(28) Dann, S. E.; Currie, D. B.; Weller, M. T.; Thomas, M. F.; Al-Rawwas, A. D. *J. Solid State Chem.* **1994**, *109*, 134.

(29) Gibb, T. C.; Matsuo, M. *J. Solid State Chem.* **1989**, *81*, 83.

(30) Battle, P. D.; Gibb, T. C.; Nixon, S. *J. Solid State Chem.* **1988**, *77*, 124.

(31) Park, S. K.; Ishikawa, T.; Tokura, Y.; Li, J. Q.; Matsui, Y. *Phys. Rev. B* **1999**, *60*, 10788.

(32) Li, J. Q.; Matsui, Y.; Park, S. K.; Tokura, Y. *Phys. Rev. Lett.* **1997**, *79*, 297.

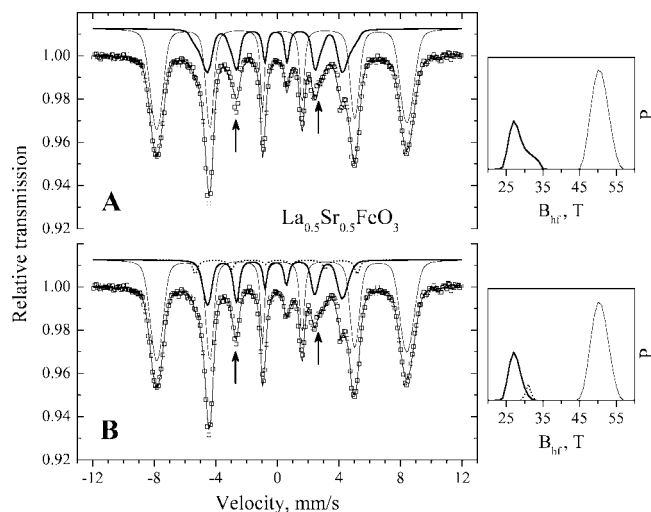


**Figure 3.** Comparison of the refinement results with two (A) and three (B) distributions of the magnetic hyperfine fields, for the Mössbauer spectrum of  $\text{La}_{0.5}\text{Sr}_{0.5}\text{FeO}_3$  at 4.1 K. The arrows indicate typical features justifying the selection of three-distribution analysis (see text).

3. Moreover, when considering only two distributions of the magnetic hyperfine fields ( $B_{\text{hf}}$ ), the distribution with lower  $B_{\text{hf}}$  is clearly bimodal (Figure 3A), showing a strong increase in isomer shift (IS) with increasing  $B_{\text{hf}}$ , which may indicate that this signal should be split into two. Introducing a third magnetic sextet is necessary to adequately describe the data on  $\text{Ln}_{0.5}\text{A}_{0.5}\text{FeO}_3$ , as found earlier<sup>22</sup> for the Pr-containing compound. As an example, Figure 3 compares the fitting results with two and three  $B_{\text{hf}}$  distributions, for  $\text{La}_{0.5}\text{Sr}_{0.5}\text{FeO}_3$  at 4.1 K. The fitting quality is, indeed, significantly improved when using the model with three distributions, which become almost symmetric (Figures 2 and 3). The refined parameters of the additional component (Table 2) are characteristic of high-spin  $\text{Fe}^{4+}$  in octahedral coordination.<sup>22,23,33,34</sup>

Within the limits of experimental uncertainty, the relative areas of  $\text{Fe}^{3+}$ ,  $\text{Fe}^{4+}$ , and  $\text{Fe}^{5+}$  distributions estimated by this model are in agreement with TGA and iodometric titration (Table 1), which confirmed that all as-prepared materials are essentially oxygen-stoichiometric. Note that, in case of stoichiometric  $\text{La}_{0.33}\text{Sr}_{0.67}\text{FeO}_3$  where the  $\text{Fe}^{4+}$  disproportionation is accompanied by a charge ordering, no evidence of the  $\text{Fe}^{4+}$  sextet is visible in the Mössbauer spectra.<sup>28–31</sup> On the other hand, the presence of moderate  $\text{Fe}^{4+}$  fractions coexisting with  $\text{Fe}^{5+}$  at low temperatures was detected in  $\text{La}_{0.33}\text{Sr}_{0.67}\text{Fe}_{1-y}\text{Co}_y\text{O}_{3-\delta}$ <sup>33</sup> and  $\text{La}_{0.5}\text{Sr}_{0.5}\text{Fe}_{1-y}\text{Al}_y\text{O}_{3-\delta}$ .<sup>23</sup> For  $\text{La}_{0.33}\text{Sr}_{0.67}\text{Fe}_{1-y}\text{Co}_y\text{O}_{3-\delta}$ , this phenomenon is associated with microscopic phase separation, implying the formation of microdomains where the charge disproportionation and ordering are suppressed.<sup>33</sup> The incorporation of B-site dopants and oxygen vacancies increasing localization of the  $\sigma^*$  ( $\text{Fe } 3d - \text{O } 2p$ ) electrons and decreasing  $\text{Sr}^{2+}$  content in  $(\text{Ln},\text{A})\text{FeO}_3$  compensated by  $\text{Fe}^{3+}$  formation are all expected to have analogous effects.<sup>34–36</sup> For instance, although the

charge disproportionation below  $T_N$  occurs in  $\text{La}_{1-x}\text{Sr}_x\text{FeO}_3$  even at low  $\text{Sr}^{2+}$  concentrations, for example,  $x = 0.3$ ,<sup>28</sup> charge ordering in  $\text{La}_{0.7}\text{Sr}_{0.3}\text{FeO}_3$  is disrupted and a charge segregation is observed.<sup>32</sup> The behavior revealed for as-prepared  $\text{Ln}_{0.5}\text{A}_{0.5}\text{FeO}_3$  can be ascribed to the same mechanisms, namely, to the charge segregation in microdomains where the local  $\text{Ln}:\text{A}$  ratio is nonideal, and/or to microscopic phase separation in the vicinity of extended defects, such as grain boundaries.

At 297 K, itinerant  $\text{Fe}^{4+}$  states disproportionating below  $T_N$  have an average-valence configuration in paramagnetic  $\text{Ln}_{0.5}\text{A}_{0.5}\text{FeO}_3$ , and a different situation takes place (Figure 4). First of all, the absorption peaks become broader and more asymmetric when the difference between  $\text{Ln}^{3+}$  and  $\text{A}^{2+}$  cation radii increases. The room-temperature spectra of  $\text{Pr}_{0.5}\text{Sr}_{0.5}\text{FeO}_3$ ,  $\text{Nd}_{0.5}\text{Sr}_{0.5}\text{FeO}_3$ , and  $\text{La}_{0.5}\text{Ba}_{0.5}\text{FeO}_3$  are adequately described by three quadrupole doublets, consistent with the analysis of 4.1 K data (Table 2). The IS values of  $\text{Fe}^{4+}$  states, which exhibit no low-temperature disproportionation, are smaller compared to the itinerant  $\text{Fe}^{4+}$ , again confirming a higher electron localization in the former case.<sup>34</sup> For  $\text{La}_{0.5}\text{Sr}_{0.5}\text{FeO}_3$ , the contribution of these localized states was found irresolvable, and the spectrum could only be fitted to two doublets. The calculated quadrupole splittings (QS) increase with increasing difference between the A-site cation radii, Figure 5A. This effect reflects rising local distortions around the iron sites and is not correlated to either average A-site cation radius, lattice symmetry, unit cell volume, or tolerance factor (Table 1). For instance, the perovskite structure of  $\text{La}_{0.5}\text{Ba}_{0.5}\text{FeO}_3$  exhibiting maximum QS was identified as cubic (space group  $Pm\bar{3}m$ ), in accordance with literature;<sup>29</sup>  $\text{La}_{0.5}\text{Sr}_{0.5}\text{FeO}_3$  has the smallest QS and a rhombohedrally distorted structure (S.G.  $R\bar{3}c$ ) at room temperature. Analogously, the tolerance factor ( $t_P$ ) is maximum for  $\text{La}_{0.5}\text{Ba}_{0.5}\text{FeO}_3$  and minimum for  $\text{Nd}_{0.5}\text{Sr}_{0.5}\text{FeO}_3$ . The corresponding  $t_P$  values calculated for the oxygen-stoichiometric ferrites using ionic radii reported by Shannon<sup>24</sup> are 1.012 and 0.967, respectively. The local distortions and strains caused by the A-site cation radius mismatch should have a strong influence on the hole localization, electronic transport, and oxygen ion diffusivity. Indeed, the highest concentration of localized  $\text{Fe}^{4+}$  states at low temperatures is observed for  $\text{La}_{0.5}\text{Ba}_{0.5}\text{FeO}_3$  (Table 2).

**3.2. Oxygen Nonstoichiometry and Hole Transport at Atmospheric Oxygen Pressure.** Other key quantities affected by the cation size mismatch relate to the average metal–oxygen bonding strength and, consequently, oxygen deficiency at elevated temperatures. To illustrate this statement, Figures 5B and 6 display the equilibrium oxygen nonstoichiometry dependencies on the difference of  $\text{Ln}^{3+}$  and  $\text{A}^{2+}$  radii in  $\text{Ln}_{0.5}\text{A}_{0.5}\text{FeO}_{3-\delta}$  and on the oxygen partial pressure, as determined by coulometric titration combined with TGA, at 1223 K. The nonstoichiometry increases with the cation radius mismatch and has minimum values for  $\text{La}_{0.5}\text{Sr}_{0.5}\text{FeO}_{3-\delta}$  in the whole  $p(\text{O}_2)$  range where the perovskite solid solutions exist (Figure 6). Again, no direct correlations with tolerance factors and structural parameters were identified. Note that a qualitatively similar decrease of the oxygen content on decreasing  $\text{A}^{2+}$  cation radius in

(33) Adler, P.; Ghosh, S. *Solid State Sci.* **2003**, *5*, 445.

(34) Adler, P.; Eriksson, S. Z. *Anorg. Allg. Chem.* **2000**, *626*, 118.

(35) Zhou, J.-S.; Goodenough, J. B. *J. Solid State Chem.* **2005**, *178*, 3679.

(36) Goodenough, J. B.; Zhou, J.-S. In *Localized to Itinerant Electronic Transition in Perovskite Oxides*; Goodenough, J. B., Eds.; Springer-Verlag: Berlin-Heidelberg, 2001; p 17.

Table 2. Parameters<sup>a</sup> Obtained from the Mössbauer Spectra of Ln<sub>0.5</sub>A<sub>0.5</sub>FeO<sub>3</sub>, Collected at 4.1 and 297 K

composition	T, K	state of iron cations	IS, mm/s	QS/ε, mm/s	B <sub>hf</sub> , T	I, %
La <sub>0.5</sub> Sr <sub>0.5</sub> FeO <sub>3</sub>	4.1	3+	0.41	-0.03	50.5	69
		4+ (localized)	0.09	-0.13	31.8	8
		5+	-0.02	-0.04	27.4	23
	297	3+	0.29	0.12		50
		4+ (itinerant + localized) <sup>b</sup>	0.10	0.09		50
Pr <sub>0.5</sub> Sr <sub>0.5</sub> FeO <sub>3</sub>	4.1	3+	0.44	-0.02	50.7	67
		4+ (localized)	0.10	-0.14	31.9	7
		5+	0.03	0.06	27.4	26
	297	3+	0.28	0.23		39
		4+ (itinerant)	0.14	0.21		53
		4+ (localized)	-0.02	0.09		8
Nd <sub>0.5</sub> Sr <sub>0.5</sub> FeO <sub>3</sub>	4.1	3+	0.43	-0.04	51.5	72
		4+ (localized)	0.11	-0.14	31.2	7
		5+	-0.04	-0.08	27.8	21
	297	3+	0.29	0.35		51
		4+ (itinerant)	0.14	0.30		41
		4+ (localized)	-0.02	0.27		8
La <sub>0.5</sub> Ba <sub>0.5</sub> FeO <sub>3</sub>	4.1	3+	0.46	-0.01	51.7	66
		4+ (localized)	0.12	-0.04	30.9	15
		5+	0.01	-0.02	26.5	19
	297	3+	0.33	0.47		48
		4+ (itinerant)	0.14	0.46		38
		4+ (localized)	0.00	0.28		14

<sup>a</sup> IS, B<sub>hf</sub>, QS, ε, and I are the isomer shift relative to metallic α-Fe at 295 K, magnetic hyperfine field, quadrupole splitting, quadrupole shift, and relative area, respectively. For the 4.1 spectra, the average IS and B<sub>hf</sub> values are given. The estimated standard deviations are <3% for I, < 0.2 T for B<sub>hf</sub>, and <0.02 mm/s for the other parameters. <sup>b</sup> See text.

perovskite-like A(Fe,Ti)O<sub>3-δ</sub> (A = Ca, Sr)<sup>37</sup> was interpreted in terms of lowering perovskite phase stability when the tolerance factor decreases, thus promoting formation of oxygen vacancy-ordered brownmillerite domains. However, Mössbauer spectroscopy of Ln<sub>0.5</sub>A<sub>0.5</sub>FeO<sub>3-δ</sub> quenched after annealing in air did not reveal any evidence of long-range vacancy ordering. The appearance of ordered microdomains in (Ln,Sr)FeO<sub>3-δ</sub> can only be detected at the oxygen partial pressures below 10<sup>-10</sup>–10<sup>-5</sup> atm; representative examples can be found elsewhere.<sup>22,38</sup> On the other hand, elastic strains in the perovskite lattice were suggested<sup>10</sup> to induce clustering of acceptor-type dopant cations and oxygen vacancies; the resultant lattice relaxation around the point-defect clusters may partly compensate stresses arising from the Ln<sup>3+</sup> and A<sup>2+</sup> size mismatch. These processes should, indeed, favor a rise of the oxygen deficiency as observed experimentally (Figure 5B). The hypothesis on strain-induced defect clustering is also in agreement with the ionic conductivity variations discussed below.

Increasing the difference between the A-site cation radii leads also to a systematic decrease of total conductivity (Figure 7A), although La<sub>0.5</sub>Ba<sub>0.5</sub>FeO<sub>3-δ</sub> exhibits higher σ values compared to Nd<sub>0.5</sub>Sr<sub>0.5</sub>FeO<sub>3-δ</sub>. The conductivity of perovskite ferrites is predominantly p-type electronic under oxidizing conditions and decreases on heating due to progressive oxygen losses, which result in lowering both the charge-carrier concentration and mobility; the latter quantity is strongly affected by decreasing concentration of Fe–O–Fe

bonds and their expansion caused by the oxygen-vacancy formation.<sup>6,8,22,23,25,36</sup> Therefore, the factors associated with the oxygen deficiency variations (Figure 5B) seem primarily responsible for the conductivity changes as a function of the A-site cation radius at high temperatures. At the same time, contributions of other relevant mechanisms cannot be neglected in the present case. In particular, increasing average size and polarizability of the A-site cations is expected to increase the overlap integral of Fe 3d – O 2p orbitals, thus increasing hole delocalization.<sup>36,39</sup> This effect, well-known for a variety of perovskite systems derived from LnMO<sub>3</sub> (M = Cr, Mn, Co),<sup>36,39,40</sup> results in relatively high hole transport in La<sub>0.5</sub>Ba<sub>0.5</sub>FeO<sub>3-δ</sub>; the conductivity of Ln<sub>0.5</sub>Sr<sub>0.5</sub>FeO<sub>3-δ</sub> decreases in the sequence La > Pr > Nd > Sm, again correlating with the A-site cation size mismatch (Figure 7A). Another necessary comment is that, at low temperatures, the higher overlap integral of Fe 3d – O 2p orbitals in La<sub>0.5</sub>Ba<sub>0.5</sub>FeO<sub>3-δ</sub> is reflected by the slightly larger isomer shifts of Fe<sup>3+</sup> states in the Ba-doped perovskite as compared to its Sr-containing analogues (Table 2). Increasing 3d electron densities leads to stronger screening of the s-orbitals and, thus, to lower electron densities at the <sup>57</sup>Fe nuclei and higher IS. Such an increase is negligible for Fe<sup>4+</sup> and Fe<sup>5+</sup> forming the metal–oxygen bonds with substantially covalent character.

**3.3. Surface-Limited Oxygen Permeation and Ionic Conductivity under Oxidizing Conditions.** Figures 8 and 9 display comparative data on the oxygen permeation fluxes and specific permeabilities, J(O<sub>2</sub>), through dense Ln<sub>0.5</sub>A<sub>0.5</sub>FeO<sub>3-δ</sub> membranes with various thicknesses. The specific oxygen permeability is related to oxygen flux density by<sup>15,18,26</sup>

(37) Kharton, V. V.; Figueiredo, F. M.; Kovalevsky, A. V.; Viskup, A. P.; Naumovich, E. N.; Jurado, J. R.; Frade, J. R. *Defect Diffus. Forum* **2000**, 186–187, 119.

(38) Kharton, V. V.; Patrakeev, M. V.; Waerenborgh, J. C.; Sobyenin, V. A.; Veniaminov, S. A.; Yaremchenko, A. A.; Gaczyński, P.; Belyaev, V. D.; Semin, G. L.; Frade, J. R. *Solid State Sci.* **2005**, 7, 1344.

(39) Ramadass, N. *Mater. Sci. Eng.* **1978**, 36, 231.

$$J(\text{O}_2) = j \cdot d \cdot \left[ \ln \left( \frac{p_2}{p_1} \right) \right]^{-1} \quad (1)$$

Because this term is proportional to  $j \times d$ , its value is thickness-independent when surface-exchange limitations are negligible but increases with thickness when they become significant.<sup>15,26</sup> The latter situation, indicating that the overall oxygen transport is governed by both the exchange kinetics and the bulk ambipolar conductivity ( $\sigma_{\text{amb}}$ ), was observed for  $\text{Ln}_{0.5}\text{Sr}_{0.5}\text{FeO}_{3-\delta}$  (Ln = La, Pr, and Nd), Figure 8. For  $\text{Nd}_{0.5}\text{Sr}_{0.5}\text{FeO}_{3-\delta}$  ceramics, the interfacial exchange limitations seem almost insignificant at 1223 K but rise on cooling as for  $\text{La}_{0.5}\text{Sr}_{0.5}\text{FeO}_{3-\delta}$  and  $\text{Pr}_{0.5}\text{Sr}_{0.5}\text{FeO}_{3-\delta}$ . In these cases, the permeation-determining factors can be estimated by an approximate relationship:<sup>41</sup>

$$\frac{1}{j} \cdot \ln \left( \frac{p_2}{p_1} \right) = \frac{16F^2d}{RT\sigma_{\text{amb}}} + k_2^{-1} + k_1^{-1} \quad (2)$$

where  $k_1$  and  $k_2$  are the exchange coefficients at the permeate and feed sides, respectively. Notice that the ambipolar conductivity is equal to  $\sigma_{\text{O}} \times \sigma_{\text{e}} / (\sigma_{\text{O}} + \sigma_{\text{e}})$ , where  $\sigma_{\text{e}}$  is the partial electronic conductivity provided by both p- and n-type charge carriers. The estimations by eq 2 demonstrated that in all cases, the ionic contribution to total conductivity under

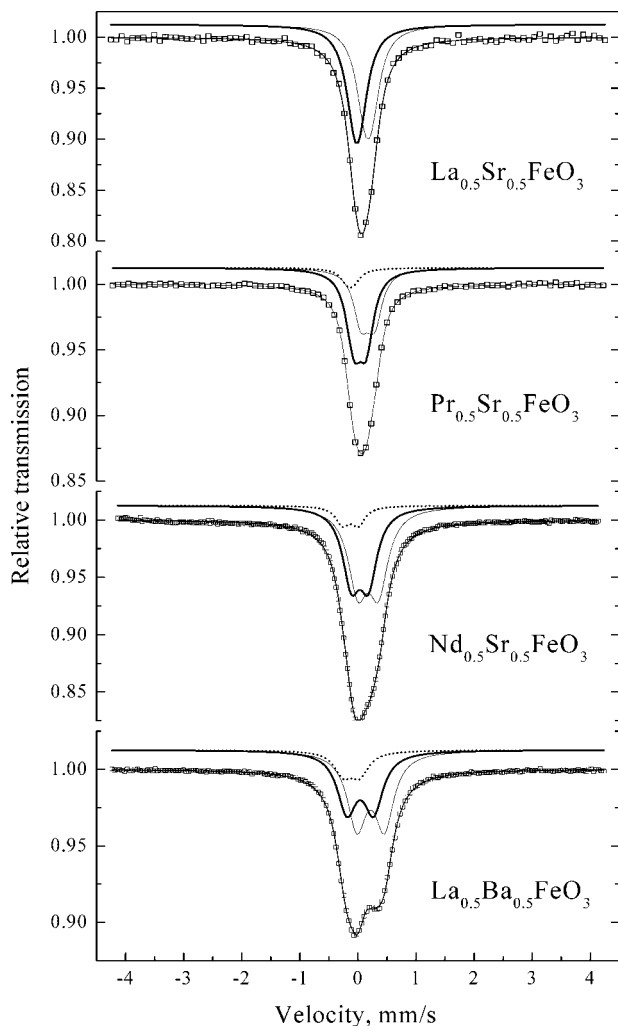


**Figure 4.** Room-temperature Mössbauer spectra of  $\text{Ln}_{0.5}\text{A}_{0.5}\text{FeO}_3$  equilibrated in air. The calculated function plotted on the experimental points is the sum of two or three doublets corresponding to octahedrally coordinated  $\text{Fe}^{3+}$  and  $\text{Fe}^{4+}$  in the itinerant and localized states.

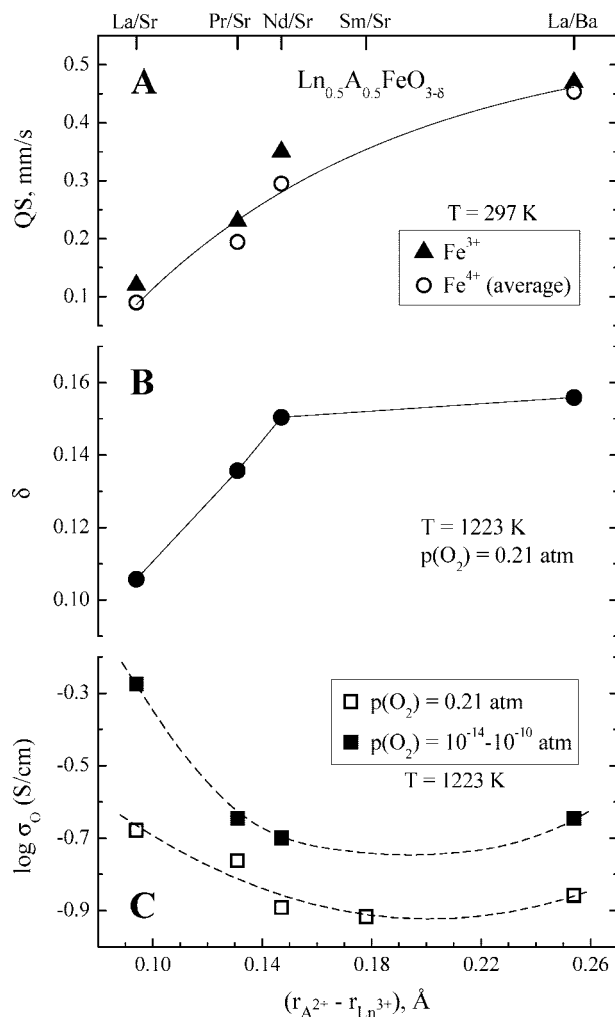


**Figure 5.** Room-temperature quadrupole splittings of  $\text{Fe}^{3+}$  and  $\text{Fe}^{4+}$  signals (A), oxygen nonstoichiometry at 1223 K and atmospheric oxygen pressure (B), and ionic conductivity values at 1223 K in air and in reducing atmospheres (C) vs the difference between  $\text{A}^{2+}$  and  $\text{Ln}^{3+}$  cation radii. The radius values<sup>34</sup> correspond to 9-fold coordination. All lines are a guide for the eye.

oxidizing conditions is lower than 0.01 and, therefore,  $\sigma_{\text{amb}} \approx \sigma_{\text{O}}$ . The same conclusion was drawn for  $\text{Sm}_{0.5}\text{Sr}_{0.5}\text{FeO}_{3-\delta}$  and  $\text{La}_{0.5}\text{Ba}_{0.5}\text{FeO}_{3-\delta}$  membranes where the specific oxygen permeability is thickness-independent within the limits of experimental error (Figure 9), showing that the oxygen transport is primarily determined by the bulk diffusion. Using the classical Wagner equation,<sup>42</sup> the ambipolar and ionic conductivities of  $\text{Sm}_{0.5}\text{Sr}_{0.5}\text{FeO}_{3-\delta}$  and  $\text{La}_{0.5}\text{Ba}_{0.5}\text{FeO}_{3-\delta}$  at atmospheric oxygen pressure were calculated as

$$\sigma_{\text{O}} \approx \sigma_{\text{amb}} = \frac{16F^2d}{RT} \cdot \left( \frac{\partial j}{\partial [\ln p_2/p_1]} \right)_{p_2/p_1-1} \quad (3)$$

The results suggest that the oxygen permeation-limiting effect of surface exchange kinetics becomes smaller when the difference between  $\text{Ln}^{3+}$  and  $\text{A}^{2+}$  radii in  $\text{Ln}_{0.5}\text{A}_{0.5}\text{FeO}_{3-\delta}$  series increases. As an example, Figure 10 compares the exchange coefficients of  $\text{Ln}_{0.5}\text{Sr}_{0.5}\text{FeO}_{3-\delta}$  (Ln = La, Pr, and Nd) ceramics at 1223 K, evaluated by eq 2. In spite of the model simplification and possible uncertainties caused by minor differences in the membrane surface microstructure and roughness, these estimations unambiguously show that the exchange rate of  $\text{Nd}_{0.5}\text{Sr}_{0.5}\text{FeO}_{3-\delta}$  is much higher than

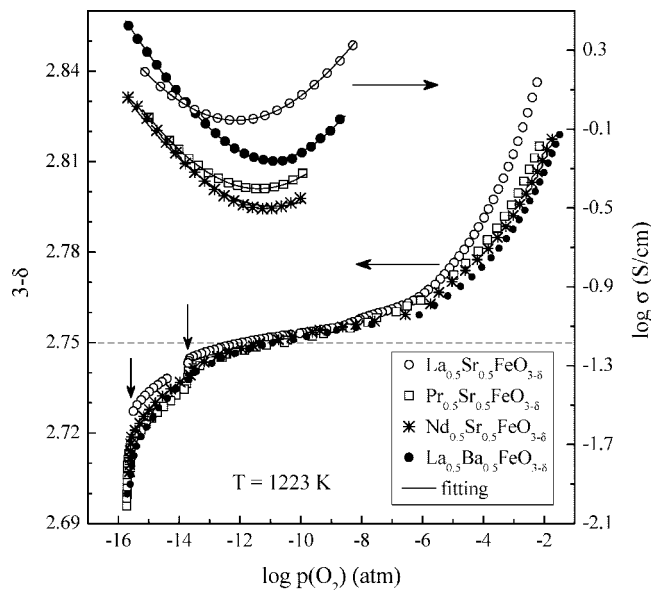


**Figure 6.** Oxygen nonstoichiometry variations in Ln<sub>0.5</sub>A<sub>0.5</sub>FeO<sub>3-δ</sub> within the studied  $p(\text{O}_2)$  range. The total conductivity variations in the vicinity of electron–hole equilibrium points are shown for comparison. The solid lines plotted on the conductivity data points correspond to fitting results using eq 4. The horizontal dashed line corresponds to the state with  $\delta = 0.25$ , when the average oxidation state of iron cations is 3+. The vertical arrows show the disorder–order transition (right) and phase decomposition (left).

that of La- and Pr-containing analogues; for Sm<sub>0.5</sub>Sr<sub>0.5</sub>FeO<sub>3-δ</sub> and La<sub>0.5</sub>Ba<sub>0.5</sub>FeO<sub>3-δ</sub>, surface limitations to the permeation fluxes are negligible. Such a correlation is in agreement with data on other perovskite-related systems (e.g., refs 17–21 and references therein) but requires additional studies to identify microscopic surface-exchange mechanisms influenced by the A-site cation size. As a first approximation, one may speculate about relationships between interfacial kinetics, surface concentration of oxygen vacancies (Figure 6), and average metal–oxygen bonding energy, which is affected by the lattice strains and should correlate with the activation barriers for oxygen sorption and incorporation into perovskite structure.<sup>43</sup>

Whatever the exchange mechanism, the oxygen ionic conduction exhibits an opposite trend, while the resultant permeation fluxes through Ln<sub>0.5</sub>Sr<sub>0.5</sub>FeO<sub>3-δ</sub> (Ln = Pr–Sm) and La<sub>0.5</sub>Ba<sub>0.5</sub>FeO<sub>3-δ</sub> membranes are quite similar (Figures 5C and 11). Notice that the values of ionic conductivity in La<sub>0.5</sub>Sr<sub>0.5</sub>FeO<sub>3-δ</sub> under oxidizing conditions (Figure 11B), its activation energy ( $E_a$ , Table 3), and oxygen fluxes (Figure 11A) are all in a reasonably good agreement with literature data on La<sub>1-x</sub>Sr<sub>x</sub>FeO<sub>3-δ</sub> where  $x = 0.4–0.5$ ,<sup>3,44,45</sup> the minor discrepancies are comparable to the effects known for

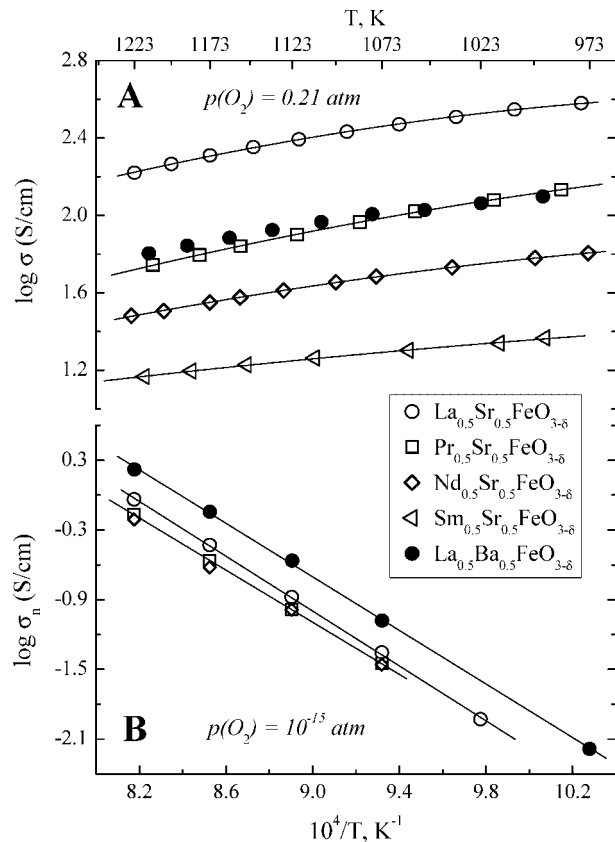


**Figure 7.** Temperature dependencies of the total conductivity of Ln<sub>0.5</sub>A<sub>0.5</sub>FeO<sub>3-δ</sub> at atmospheric oxygen pressure (A) and n-type electronic conductivity at  $p(\text{O}_2) = 10^{-15}$  atm (B).

microstructural differences.<sup>7</sup> For comparison, the activation energy for ion diffusion in La<sub>0.5</sub>Sr<sub>0.5</sub>FeO<sub>3-δ</sub> was reported as  $129 \pm 13$  kJ/mol at 1060–1220 K.<sup>3</sup> The apparent activation energy for the bulk-limited oxygen permeation through La<sub>0.5</sub>Sr<sub>0.5</sub>FeO<sub>3-δ</sub> membranes was  $101 \pm 6$  kJ/mol at 1150–1250 K, but increased up to  $209 \pm 7$  kJ/mol on cooling down to 1050 K when extensive vacancy-ordering processes start.<sup>44</sup> For (La<sub>0.6</sub>Sr<sub>0.4</sub>)<sub>0.99</sub>FeO<sub>3-δ</sub> where the oxygen deficiency and ionic conductivity are both lower and the vacancy formation enthalpy contribution to the activation energy is higher, the average  $E_a$  for ionic conduction at 1070–1270 K was determined as 156 kJ/mol.<sup>45</sup> This level of coincidence, and qualitatively similar relationships between the oxygen permeability of La<sub>0.8</sub>A<sub>0.2</sub>FeO<sub>3-δ</sub> (A = Ca, Sr, Ba) and A-site cation radii,<sup>46</sup> seem to validate major conclusions drawn in the present work.

It should be separately stressed that the decrease of intrinsic ionic conduction due to increasing A-site cation size mismatch in Ln<sub>0.5</sub>A<sub>0.5</sub>FeO<sub>3-δ</sub> (Figure 5) is observed when the oxygen deficiency increases, thus providing additional supporting evidence for the hypothesis<sup>10</sup> on strain-induced clustering of oxygen vacancies. This hypothesis agrees also with variations of the anion conductivity activation energy, which tends to increase with the A-site cation radius difference (Table 3). Raising the activation energy on cooling below 1120 K is associated,

(40) Kharton, V. V.; Yaremchenko, A. A.; Naumovich, E. N. *J. Solid State Electrochem.* **1999**, *3*, 303.

(41) Marozau, I.; Kharton, V.; Viskup, A.; Frade, J.; Samakhval, V. *J. Eur. Ceram. Soc.* **2006**, *26*, 1371.

(42) Bouwmeester, H. J. M.; Burggraaf, A. J. In *Fundamentals of Inorganic Membrane Science and Technology*; Burggraaf, A. J., Cot, L., Eds.; Elsevier: Amsterdam, 1996; p 435.

(43) Adler, S. B.; Chen, X. Y.; Wilson, J. R. *J. Catal.* **2007**, *245*, 91.

(44) Bayraktar, D.; Diethelm, S.; Holtappels, P.; Graule, T.; Van herle, J. *J. Solid State Electrochem.* **2006**, *10*, 589.

(45) Sogaard, M.; Hendriksen, P. V.; Mogensen, M. *J. Solid State Chem.* **2007**, *180*, 1489.

(46) Bidrawn, F.; Lee, S.; Vohs, J. M.; Gorte, R. J. *J. Electrochem. Soc.* **2008**, *155*, B660.

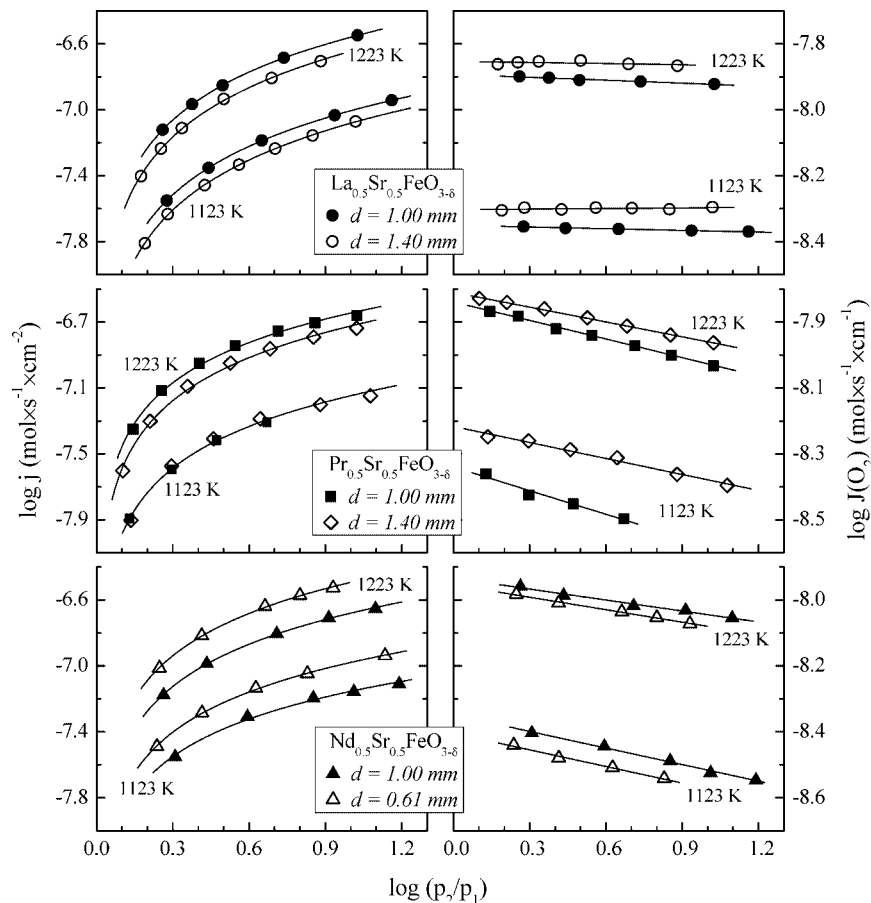


**Figure 8.** Dependence of the oxygen permeation fluxes (left) and specific oxygen permeability (right) of dense  $\text{Ln}_{0.5}\text{Sr}_{0.5}\text{FeO}_{3-\delta}$  ( $\text{Ln} = \text{La-Nd}$ ) ceramic membranes on the oxygen partial pressure gradient. The feed-side oxygen pressure ( $p_2$ ) is 0.21 atm.

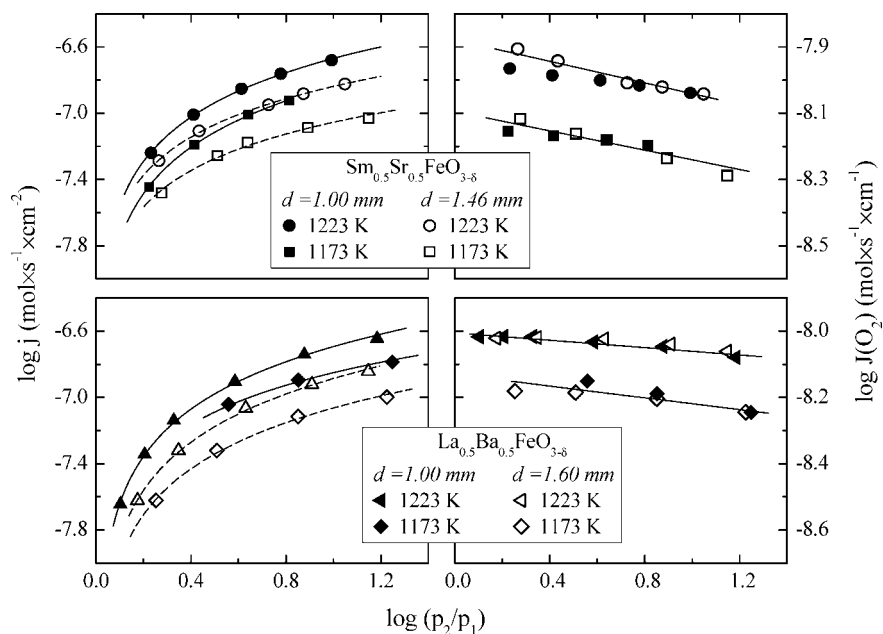


**Figure 9.** Dependence of the oxygen permeation fluxes (left) and specific oxygen permeability (right) of  $\text{Sm}_{0.5}\text{Sr}_{0.5}\text{FeO}_{3-\delta}$  and  $\text{La}_{0.5}\text{Ba}_{0.5}\text{FeO}_{3-\delta}$  ceramic membranes on the oxygen partial pressure gradient. The feed-side oxygen pressure ( $p_2$ ) is 0.21 atm.

again, with progressive vacancy trapping.<sup>42</sup> The concentration of mobile oxygen vacancies in  $\text{Ln}_{0.5}\text{A}_{0.5}\text{FeO}_{3-\delta}$  under oxidizing conditions seems substantially low; as a result, even moderate increase of the oxygen partial pressure decreases ionic transport (inset in Figure 10).

Another necessary comment is that nonlinearity of the  $\sigma_{\text{O}}$  versus cation size dependencies (Figure 5C) makes it impossible to consider local distortions in the perovskite lattice, which should be maximal for  $\text{La}_{0.5}\text{Ba}_{0.5}\text{FeO}_{3-\delta}$ , among the most critical aspects determining anion diffusivity. In fact, the ionic

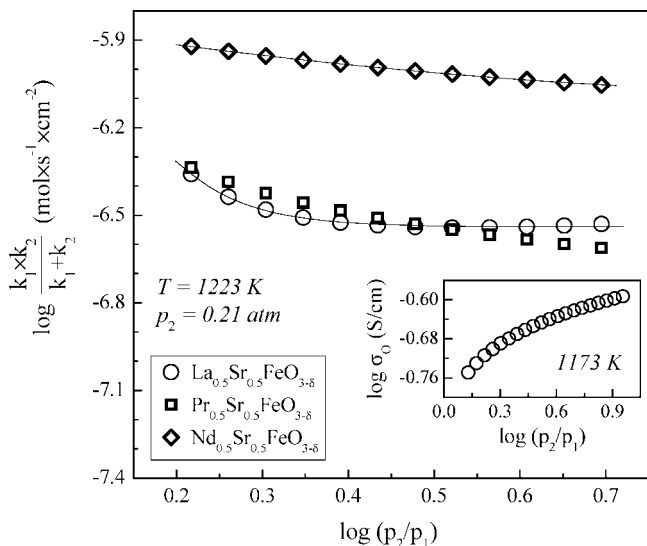


**Figure 10.** Example of the surface exchange coefficients of  $\text{Ln}_{0.5}\text{Sr}_{0.5}\text{FeO}_{3-\delta}$  ( $\text{Ln} = \text{La}-\text{Nd}$ ), estimated by eq 2 from the oxygen permeation data. Inset shows the calculated ionic conductivity of  $\text{La}_{0.5}\text{Sr}_{0.5}\text{FeO}_{3-\delta}$ , averaged under the oxygen partial pressure gradient, at 1173 K.

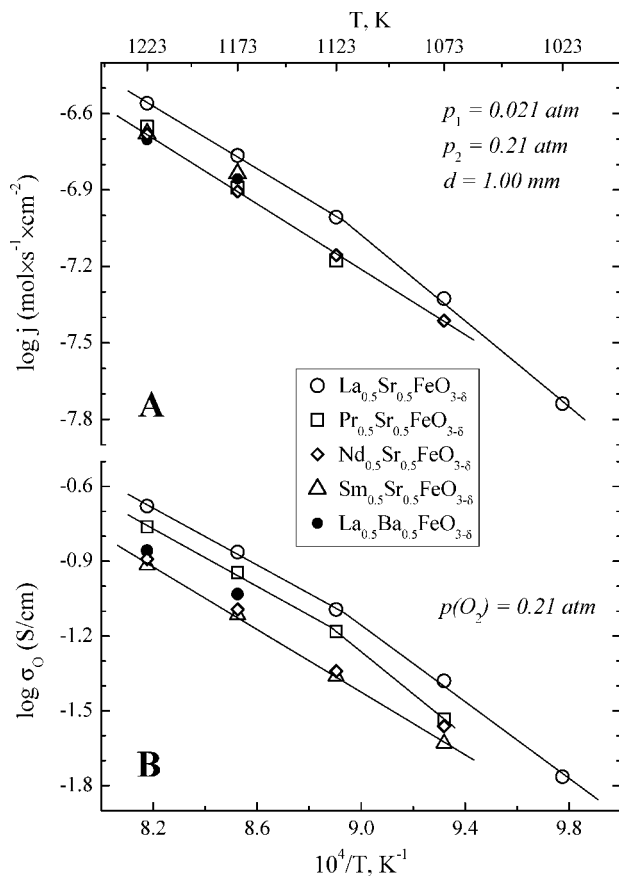


**Figure 11.** Temperature dependencies of the oxygen permeation fluxes through  $\text{Ln}_{0.5}\text{A}_{0.5}\text{FeO}_{3-\delta}$  membranes under fixed oxygen partial pressure gradient (A) and oxygen ionic conductivity at atmospheric oxygen pressure (B). Solid lines are for visual guidance only.

conductivity of  $\text{La}_{0.5}\text{Ba}_{0.5}\text{FeO}_{3-\delta}$  is higher than that of  $\text{Ln}_{0.5}\text{Sr}_{0.5}\text{FeO}_{3-\delta}$  ( $\text{Ln} = \text{Nd}$ ,  $\text{Sm}$ ), suggesting a relevant impact of the A-site cation polarizability. On the contrary, the values of tolerance factor calculated accounting for the iron oxidation states at 1223 K and atmospheric oxygen pressure (Figure 6) are 0.976 for  $\text{La}_{0.5}\text{Sr}_{0.5}\text{FeO}_{3-\delta}$  and 0.958 for  $\text{Nd}_{0.5}\text{Sr}_{0.5}\text{FeO}_{3-\delta}$ ,

both being close enough to 0.96–0.97 reported as an optimum level.<sup>11,16</sup> The latter relationship may invalidate the approach<sup>11,16</sup> based on tolerance factor analysis, for optimization of oxygen ionic transport in ferrite-based materials.

**3.4. Behavior in Reducing Atmospheres.** Figure 6 displays representative examples of the  $p(\text{O}_2)$  dependencies of oxygen nonstoichiometry in the whole oxygen pressure range where perovskite-like  $\text{Ln}_{0.5}\text{A}_{0.5}\text{FeO}_{3-\delta}$  exist, at 1223 K. The main trends are well-known for ferrite-based solid solutions.<sup>3,6,24,38,42</sup> In oxidizing atmospheres, decreasing oxygen partial pressure results in extensive oxygen losses. Then the nonstoichiometry approaches a plateau in the vicinity of so-called electron–hole equilibrium points ( $\delta \rightarrow 0.25$ ), where the average oxidation state of iron becomes 3+. The latter was confirmed by the Mössbauer spectroscopy analysis of reduced  $\text{Ln}_{0.5}\text{A}_{0.5}\text{FeO}_{3-\delta}$ . One example is presented in the inset of Figure 1B, which shows the Mössbauer spectrum of  $\text{La}_{0.5}\text{Ba}_{0.5}\text{FeO}_{2.75}$  quenched after reduction; the spectrum reveals only the presence of  $\text{Fe}^{3+}$  cations in 6-, 5-, and 4-fold coordination.

When the average oxidation state of iron is 3+, the partial p-type and n-type electronic conductivities are nearly equal and the total conductivity versus  $p(\text{O}_2)$  isotherms exhibit characteristic minima, Figure 6. Further reduction leads to a stepwise decrease of the oxygen content when a massive transformation into vacancy-ordered modification occurs,<sup>22,38</sup> followed by phase decomposition reflected by another dramatic drop of the oxygen stoichiometry. The oxygen chemical potentials corresponding to these transitions are marked in Figure 6 by the vertical arrows. As the oxygen vacancy concentration around the electron–hole equilibrium points is almost constant, the ionic conductivity is essentially  $p(\text{O}_2)$ -independent; the concentrations of n- and p-type electronic charge carriers can be considered proportional to  $p(\text{O}_2)^{-1/4}$  and  $p(\text{O}_2)^{1/4}$ , respectively.<sup>3,42</sup> Consequently, the total conductivity variations in this  $p(\text{O}_2)$  range can be approximated by the classical model

$$\sigma = \sigma_o + \sigma_n^0 \cdot p(\text{O}_2)^{-1/4} + \sigma_p^0 \cdot p(\text{O}_2)^{1/4} \quad (4)$$

where  $\sigma_n^0$  and  $\sigma_p^0$  are the values of partial n- and p-type electronic conductivities ( $\sigma_n$  and  $\sigma_p$ ) at unit oxygen pressure. The fitting results shown by solid lines in Figure 6 are in excellent agreement with experimental data; the minor deviations originate from slight changes in the vacancy concentration and partial ionic conductivity on reduction.

The anion conduction under reducing conditions (Figures 5C and 12) becomes substantially higher with respect to atmospheric air but displays a very similar dependence on the A-site cation size. Moreover, no direct proportionality between the anion transport and oxygen deficiency variations with decreasing  $p(\text{O}_2)$  can be again revealed. In fact, the increase of ionic conductivity on reduction is considerably larger than expected assuming  $p(\text{O}_2)$ -independent vacancy diffusion coefficients and negligible vacancy trapping. These tendencies confirm that a significant fraction of oxygen vacancies in  $\text{Ln}_{0.5}\text{A}_{0.5}\text{FeO}_{3-\delta}$  are essentially immobile due to clustering promoted by

**Table 3. Activation Energies for the Oxygen Ionic and n-Type Electronic Transport in  $\text{Ln}_{0.5}\text{A}_{0.5}\text{FeO}_{3-\delta}$** 

composition	oxygen ionic conduction				n-type electronic transport	
	$p(\text{O}_2) = 0.21 \text{ atm}$		$p(\text{O}_2) = 10^{-14} - 10^{-10} \text{ atm}$		$p(\text{O}_2) = 10^{-15} \text{ atm}$	
	$T, \text{K}$	$E_a, \text{kJ/mol}$	$T, \text{K}$	$E_a, \text{kJ/mol}$	$T, \text{K}$	$E_n, \text{kJ/mol}$
$\text{La}_{0.5}\text{Sr}_{0.5}\text{FeO}_{3-\delta}$	1123–1223	109 ± 19	1023–1223	58 ± 3	1023–1223	226 ± 8
	973–1123	147 ± 16				
$\text{Pr}_{0.5}\text{Sr}_{0.5}\text{FeO}_{3-\delta}$	1123–1223	111 ± 22	1073–1223	64 ± 9	1073–1223	215 ± 3
	1073–1123	162				
$\text{Nd}_{0.5}\text{Sr}_{0.5}\text{FeO}_{3-\delta}$	1073–1223	113 ± 13	1073–1223	96 ± 13	1073–1223	207 ± 17
$\text{Sm}_{0.5}\text{Sr}_{0.5}\text{FeO}_{3-\delta}$	1073–1223	127 ± 8				
$\text{La}_{0.5}\text{Ba}_{0.5}\text{FeO}_{3-\delta}$	1173–1223	105	973–1223	70 ± 6	973–1223	230 ± 9

the A-site cation radius mismatch. Consequently, when the concentration of ionic charge carriers increases on reducing  $p(\text{O}_2)$ , the contribution of vacancy-formation enthalpy to the apparent activation energies for ionic transport becomes smaller and the  $E_a$  values decrease down to the level characteristic of solid oxide electrolytes, 58–96 kJ/mol (Table 3).

Regardless of the microscopic mechanisms, the data on ionic transport show that the incorporation of  $\text{Ba}^{2+}$  and/or lanthanide cations with moderate radius (Pr, Nd, Sm) into the perovskite lattice of mixed-conducting ferrites should indeed increase the electrochemical activity of porous ferrite-based electrodes in SOFCs and other solid-electrolyte devices, but may have a negative impact on the performance of dense ceramic membranes made of these materials. Nevertheless, such doping strategies seem still preferable for the development of porous catalytic layers applied onto the ceramic membrane surface. The same conclusions can be drawn for potential use of mixed rare-earth precursors.

Finally, Figure 7B compares the partial n-type electronic conductivities of  $\text{Ln}_{0.5}\text{A}_{0.5}\text{FeO}_{3-\delta}$  at  $p(\text{O}_2) = 10^{-15} \text{ atm}$ , calculated subtracting the oxygen-ionic and hole contributions from total conductivity. In contrast to the oxygen-ionic and hole transport, the n-type electronic conduction tends to increase with the average A-site cation radius and perovskite tolerance factor. Most likely, this trend originates from extensive formation and growth of the

vacancy-ordered domains at low oxygen chemical potentials, as reflected by the anomalies in the  $\delta$  versus  $p(\text{O}_2)$  curves (Figure 6), although the average perovskite-type structure is retained (Figure 1B). Lowering tolerance factors is expected to decrease thermodynamic stability of the perovskite phases, thus promoting long-range vacancy ordering in the oxygen sublattice. Although the latter relationships require further validation, this hypothesis seems supported by the fact that the quadrupole shift of tetrahedrally coordinated  $\text{Fe}^{3+}$ , refined from the Mössbauer spectrum of reduced  $\text{La}_{0.5}\text{Ba}_{0.5}\text{FeO}_{2.75}$  (inset in Figure 1,  $\varepsilon = 0.12 \text{ mm/s}$ ), is considerably lower than that of  $\text{Pr}_{0.5}\text{Sr}_{0.5}\text{FeO}_{2.75}$  (0.44 mm/s).<sup>22</sup> Irrespective of the vacancy-ordering processes, the activation energies for n-type electronic conduction ( $E_n$ ) in  $\text{Ln}_{0.5}\text{A}_{0.5}\text{FeO}_{3-\delta}$  are close to one another within the limits of statistical error, Table 3. For perovskite-related ferrite materials, the  $E_n$  values correlate often with the phase decomposition enthalpy in reducing atmospheres, since these quantities are both determined by the iron–oxygen bond energy.<sup>47</sup> Indeed, the nonstoichiometry data (Figure 6) indicate that the low- $p(\text{O}_2)$  stability limits of  $\text{Ln}_{0.5}\text{A}_{0.5}\text{FeO}_{3-\delta}$  are similar in all cases.

#### 4. Conclusions

The effects of A-site cation size on the oxygen nonstoichiometry, p- and n-type electronic transport, oxygen permeability, partial ionic conductivity, and low- $p(\text{O}_2)$  stability of perovskite-like  $\text{Ln}_{0.5}\text{A}_{0.5}\text{FeO}_{3-\delta}$  ( $\text{Ln} = \text{La} - \text{Sm}$ ;  $\text{A} = \text{Sr}, \text{Ba}$ ) at elevated temperatures have been appraised. The oxygen deficiency was found to increase with the difference between  $\text{Ln}^{3+}$  and  $\text{A}^{2+}$  cation radii, while the anion conduction exhibits an opposite tendency, suggesting important influence of oxygen-vacancy trapping processes induced by the lattice strain. At low temperatures when  $\text{Ln}_{0.5}\text{A}_{0.5}\text{FeO}_3$  becomes oxygen-stoichiometric, similar relationships are observed between the cation size mismatch and quadrupole splittings derived from the Mössbauer spectra. The activation energy for ionic conductivity, calculated from the oxygen permeation and total conductivity data at 973–1223 K, decreases from 105–162 kJ/mol in air down to 58–96 kJ/mol in reducing atmospheres due to lowering contribution of the vacancy-formation enthalpy. Because of the strain-induced oxygen nonstoichiometry variations, the A-site cation radius mis-

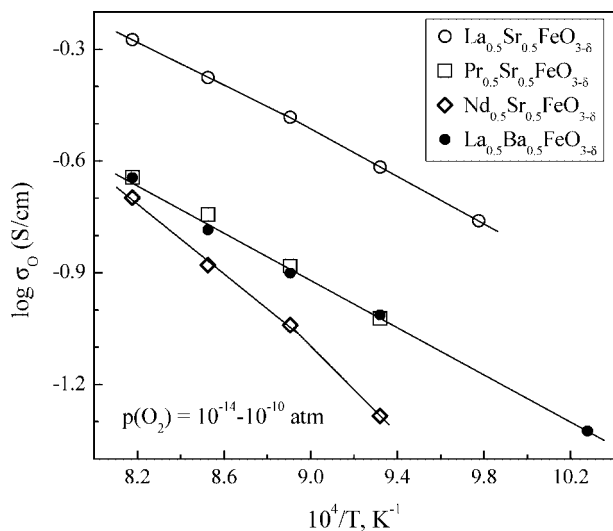


**Figure 12.** Temperature dependence of the oxygen-ionic conductivity of  $\text{Ln}_{0.5}\text{A}_{0.5}\text{FeO}_{3-\delta}$  calculated from the  $p(\text{O}_2)$  dependencies of the total conductivity under reducing conditions.

(47) Patrakeev, M. V.; Leonidov, I. A.; Kozhevnikov, V. L.; Kharton, V. V. *Solid State Sci.* **2004**, *6*, 907.

match correlates apparently with the hole conduction predominant under oxidizing conditions. However, the partial p- and n-type electronic conductivities of  $Ln_{0.5}A_{0.5}FeO_{3-\delta}$  depend also on numerous other factors, such as the average radius and polarizability of A-site cations. The membrane thickness dependencies of steady-state oxygen fluxes through dense  $Ln_{0.5}A_{0.5}FeO_{3-\delta}$  ceramics indicate that the role of surface exchange kinetics as a permeation-limiting factor tends to decrease on  $Ba^{2+}$

doping and on decreasing  $Ln^{3+}$  size, again correlating with the lattice strains.

**Acknowledgment.** This work was supported by the FCT, Portugal (Project Nos. PTDC/CTM/64357/2006, SFRH/BPD/28629/2006, and SFRH/BPD/28913/2006), by the Belgian Federal Science Policy foundation, and by the Belarus Ministry of Education.

CM801569J